1
2

Continental-scale contributions to the global CFC-11 emission increase between 2012 and 2017

3
4

5 Lei Hu[1,2], Stephen A. Montzka[2], Fred Moore[1,2], Eric Hintsa[1,2], Geoff Dutton[1,2], M. Carolina Siso[1,2],
6 Kirk Thoning[2], Robert W. Portmann[3], Kathryn McKain[1,2], Colm Sweeney[2], Isaac Vimont[1,2], David
7 Nance[1,2], Bradley Hall[2], Steven Wofsy[4]

8
9 [1] Cooperative Institute for Research in Environmental Sciences, University of Colorado-Boulder,
10 Boulder, CO, USA
11 [2] Global Monitoring Laboratory, NOAA, Boulder, CO, USA
12 [3] Chemical Science Laboratory, NOAA, Boulder, CO, USA
13 [4] Department of Earth and Planetary Sciences, Harvard University, Boston, MA, USA

14
15 *Correspondence to*: Lei Hu (lei.hu@noaa.gov)

16

17 **Abstract.** The detection of increasing global CFC-11 emissions after 2012 alerted society to a
18 possible violation of the Montreal Protocol on Substances that Deplete the Ozone Layer (MP).
19 This alert resulted in parties to the MP taking urgent actions. As a result, atmospheric
20 measurements made in 2019 suggest a sharp decline in global CFC-11 emissions. Despite the
21 success in the detection and mitigation of part of this problem, regions fully responsible for the
22 recent global emission changes of CFC-11 have not yet been identified. Roughly two thirds (60 ±
23 40 %) of the emission increase between 2008 - 2012 and 2014 - 2017 and two thirds (60 ± 30 %)
24 of the decline between 2014 - 2017 and 2019 were explained by regional emission changes in
25 eastern mainland China. Here, we used atmospheric CFC-11 measurements made from two global
26 aircraft surveys, the HIAPER Pole-to-Pole Observations (HIPPO) in November 2009 – September
27 2011 and the Atmospheric Tomography Mission (ATom) in August 2016 – May 2018, in
28 combination with the global CFC-11 measurements made by the US National Oceanic and
29 Atmospheric Administration during these two periods, to derive global and regional emission
30 changes of CFC-11. Our results suggest Asia accounted for the largest fractions of global CFC-
31 11 emissions in both periods, 43 (37 – 52) % during November 2009 – September 2011 and 57
32 (49 – 62) % during August 2016 – May 2018. Asia was also primarily responsible for the emission
33 increase between these two periods, accounting for 86 (59 – 115) % of the global CFC-11 emission
34 rise between the two periods. Besides eastern mainland China, temperate western Asia and
35 tropical Asia also contributed significantly to global CFC-11 emissions during both periods and
36 likely to the global CFC-11 emission increase. The atmospheric observations further provide
37 strong constraints on CFC-11 emissions from North America and Europe, suggesting that each of
38 them accounted for 10 – 15 % of global CFC-11 emissions during the HIPPO period and smaller
39 fractions in the ATom period. For South America, Africa, and Australia, the derived regional
40 emissions had larger dependence on the prior assumptions of emissions and emission changes, due
41 to a lower sensitivity of the observations considered here to emissions from these regions.
42 However, significant increases in CFC-11 emissions from southern hemispheric lands were not
43 likely due to the observed increase of north-to-south interhemispheric gradients in atmospheric
44 CFC-11 mole fractions from 2012 to 2017.

45

46 **1. Introduction**
47   Trichlorofluoromethane, CFC-11, is a potent ozone depleting substance, whose production
48 has been controlled by the Montreal Protocol since 1987. By 2010, reported global production
49 and consumption of CFC-11 was near zero (United Nations Environment Programme (UNEP),
50 2021a, b). Corresponding to the declining production and consumption, global emissions of CFC-
51 11 declined between 1988 and 2012. By 2012, the global CFC-11 emission magnitude was 50 –
52 80 Gg yr^{-1} with this range being associated primarily with its uncertain atmospheric lifetime (Engel
53 et al., 2018). The remaining emissions of CFC-11 were primarily from existing equipment and
54 insulation foams, known as "CFC-11 banks". However, a large increase of global CFC-11
55 emission from 2012 – 2017 was discovered (Montzka et al., 2018; Rigby et al., 2019; Montzka et
56 al., 2021), suggesting illicit CFC-11 production despite the global ban on production and
57 consumption under the MP beginning in 2010. This surprisingly large increase of CFC-11
58 emissions attracted great attention from scientists, policy makers, and industrial experts around the
59 world (Montzka et al., 2018; Rigby et al., 2019; Dhomse et al., 2019; Ray et al., 2020; Adcock et
60 al., 2020; Keeble et al., 2020; Chen et al., 2020), who sought information to enable rapid mitigation
61 of the unexpectedly enhanced CFC-11 emissions and ensure no significant delay in the recovery
62 of stratospheric ozone. Despite the international effort to understand the origin of this large global
63 emission increase of CFC-11, only a portion of the emission rise (60 ± 40 %) could be explained
64 by emission increases from eastern mainland China (Rigby et al., 2019; Adcock et al., 2020; Park
65 et al., 2021). It remains unclear where the rest of the global CFC-11 emission increase originated.
66   Following the initial studies and announcements of anomalous CFC-11 emission increases,
67 a surprisingly sharp decline in global CFC-11 emissions occurred from 2018 to 2019 (Montzka et
68 al., 2021). This decline immediately followed the global emission rise and had a similar magnitude
69 as the emission rise between 2012 and 2017, resulting in global CFC-11 emissions in 2019 being
70 similar to the mean 2008 – 2012 value (Montzka et al., 2021). Interestingly, roughly the same
71 proportion of this emission decrease (60 ± 30 %) can be explained by an emission drop in eastern
72 mainland China (Park et al., 2021) during this period, similar to the contribution of eastern
73 mainland China to the global CFC-11 emission rise earlier (60 ± 40 %).
74   In this study, we analyzed global CFC-11 measurements made from the HIAPER Pole-to-
75 Pole Observations (HIPPO) in November 2009 – September 2011, the Atmospheric Tomography
76 Mission (ATom) in August 2016 – May 2018 (Wofsy, 2018; Bourgeois et al., 2020) and concurrent
77 CFC-11 measurements from the US National Oceanic and Atmospheric Administration (NOAA)
78 global atmospheric sampling network (Montzka et al., 2018) and combined them with Lagrangian-
79 based inverse modeling techniques (Hu et al., 2017) to quantify continental- and regional- scale
80 CFC-11 emission estimates between both periods. Coincidentally, the timing of the HIPPO and
81 ATom campaigns covered the periods when the global CFC-11 emissions were at the minimum
82 and maximum before the CFC-11 emission decline in 2018 – 2019. Hereafter, we will refer
83 November 2009 – September 2011 as the HIPPO period and August 2016 – May 2018 as the
84 ATom period. Here we further investigate regional contributions to the global CFC-11 emission
85 rise between these two periods.
86
87 **2. Methods**
88 **2.1. Overview**
89   To infer regional CFC-11 emissions from observed atmospheric mole fractions, we used a
90 Bayesian inverse modeling framework following the method described in previous studies (Hu et
91 al., 2015; Hu et al., 2017; Hu et al., 2016). In brief, the inverse modeling method assumes a linear

2

92   relationship between measured atmospheric mole fraction enhancements and emissions upwind of
93   the measurement locations. The linear operator, termed footprint, is the sensitivity of atmospheric
94   mole fraction enhancements to upwind emissions, and it was computed for each sample using the
95   Hybrid Single Particle Lagrangian Integrated Trajectory (HYSPLIT) model described in Stein et
96   al. (2015). Bayesian inverse models (Rodgers, 2000) require initial assumptions about the
97   magnitudes and distributions of emissions, or prior emissions. By assuming that errors between
98   the "true" and prior emissions and errors between atmospheric mole fraction observations and
99   simulated mole fractions (using the computed footprints) follow Gaussian distributions, we
100   construct a cost function (*L*) (Eq. 1) based on Bayes' Theorem:

101
$$L = \frac{1}{2}(z - Hs)^T R^{-1}(z - Hs) + \frac{1}{2}\left(s - s_p\right)^T Q^{-1}\left(s - s_p\right) \tag{1}$$

102   where, z represents the observed atmospheric enhancement relative to the upwind background
103   atmosphere (Section 2.2.3). s_p and s represent the prior and posterior CFC-11 emissions. *H*
104   represents the Jacobian matrix or the first-order partial derivatives of z to s. *R* and *Q* stand for the
105   model-data mismatch covariance and prior flux error covariance. The values given to R and Q
106   determine the relative weight between the prior emission assumptions and atmospheric
107   observations in the final solution. Here, we used the maximum likelihood estimation method (Hu
108   et al., 2015; Michalak et al., 2005) and atmospheric observations to directly solve for site-
109   dependent model-data mismatch errors and prior flux errors. For the aircraft campaigns (HIPPO
110   and ATom), we derive separate model-data mismatch errors, one for each campaign.
111

2.2. Inversions for the HIPPO and ATom time intervals

113   In this section, we describe the detailed observation selection, estimating background mole
114   fractions that were pre-subtracted from atmospheric observations before inversions, and prior
115   emission assumptions for the global inversion we conducted for the HIPPO period (November
116   2009 – September 2011) and the ATom period (August 2016 – May 2018) using a Lagrangian
117   inverse modeling approach.
118

2.2.1. CFC-11 measurements and data selection for global inversion analyses

120   All the CFC-11 measurements considered in our global inversion were made by the Global
121   Monitoring Laboratory, NOAA, through four different sampling and measurement programs: the
122   global aircraft surveys (flask samples collected during HIPPO and ATom), a global weekly surface
123   flask sampling program, a global in situ sampling program, and a biweekly to monthly aircraft
124   profiling sampling program primarily in North America (Fig. 1). CFC-11 measurements for the
125   ATom campaigns were primarily made by a gas chromatography and mass spectrometry (GCMS)
126   instrument (named "M3") that was also dedicated for flask-air measurements in the global weekly
127   surface flask program. Flask-air samples collected from the biweekly to monthly aircraft profiling
128   sampling program and from the HIPPO campaign were analyzed by another dedicated GCMS
129   instrument called "M2" and later upgraded to "PR1" in Sep 2014. Hourly in situ CFC-11
130   measurements were made by in situ gas chromatography with electron capture detector
131   instruments (GC-ECDs) located at individual observatories (the Chromatograph for Atmospheric
132   Trace Species, CATS). All the NOAA CFC-11 measurements were referenced to the same
133   calibration scale (NOAA-2016) and suite of primary gravimetric standards. However, small
134   differences were observed between results from the analysis of the same flask-air samples on two
135   different instruments (i.e., median differences: 0.7% between M3 and M2 during the HIPPO period
136   and 0.9% between M3 and PR1 during ATom period; Fig. S1), and between results from samples

137 collected within ±2 hours that were analyzed by M3 (from flasks) and CATS (from in situ
138 instrumentation) (median differences were < 0.2% during the HIPPO and ATom periods at three
139 relevant sites; Fig. S1). To minimize the influence of these artificial differences on derived fluxes,
140 particularly because the atmospheric CFC-11 signals associated with changing emissions were
141 extremely small (Montzka et al., 2021; Montzka et al., 2018), results from M2 and PR1 were scaled
142 to those from M3. Scaling factors were calculated over 3-month intervals for M2 and PR1 to make
143 them consistent for the same air-sample analyses. For the CATS measurements, fewer comparison
144 points were available, so scale adjustments of CATS data to M3 were based on one scaling factor
145 per site for the HIPPO period and, separately, the ATom period.

146   For measurements made during the HIPPO and ATom campaigns, we only include
147 measurements below 8 km in the global inversions to minimize the influence of stratospheric loss
148 on measured mole fractions and because high altitude samples typically have less emission
149 information. Some samples obtained below 8 km still retained a notable stratospheric loss signal,
150 and these data were also removed from further considerations on the basis of reduced mole
151 fractions observed for N_2O, which is useful for tracing stratospheric influence in an air parcel
152 owing to its small atmospheric variability and high-precision measurements.

153   For data obtained in NOAA's regular flask-air sampling programs, the inversions included
154 results from sites that are relatively far from recent anthropogenic emissions (i.e. sites many miles
155 away from populated areas or that are not situated in the boundary layer), in order to capture
156 emissions from broad regions. These observations include the weekly surface flask sampling at
157 remote, globally-distributed locations (Fig. 1) and aircraft profiling in Cook Islands and Alaska,
158 US, and above 1 km (above ground) over the contiguous US (Fig. 1). Most of our aircraft profiling
159 sampling was below 8 km above sea level.

160   To reduce the extremely large computing cost of footprint calculations for surface in situ
161 sampling, we chose a subset of in situ samples for inversion analyses. We randomly selected one
162 sample per day from sites such as Barrow, Alaska, US (BRW) and Tutuila, American Samoa
163 (SMO), and one daytime sample and one nighttime sample each day at Mauna Loa Observatory,
164 Hawaii, US (MLO). In situ measurements made at Summit, Greenland (SUM) were excluded due
165 to poorer precision of CFC-11 measurements made at this station.

166   Although many of the observations we used were from remote Pacific and Atlantic Oceans
167 locations, or from the free troposphere over North America, they did contain above-zero sensitivity
168 to emissive signals transported from all the continents, as shown in their footprints (Fig. 1); but
169 the overall sensitivity to emissions from South America, southern Africa, and Australia is low
170 relative to North American, Europe, and Asia (Fig. 1). Thus, observational constraints on
171 emissions from North America, Europe, and Asia are stronger and are less dependent on prior
172 assumptions compared to those from South America, Africa, and Australia.

173 **2.2.2. Footprint simulations**
174   We used the HYSPLIT model driven by the global data assimilation system at a 0.5°
175 resolution (GDAS0.5°), to simulate footprints for our global inversion analyses. To determine an
176 adequate number of particles needed for this global simulation, we tested running HYSPLIT
177 backward for 45 days using 5000 and 10000 particles for a subset of observations obtained from
178 the second campaign during ATom (ATom-2). We compared the footprints from these two
179 independent simulations, which are only different by < 0.05% in the total summed sensitivities.
180 Footprint distributions and magnitudes in individual time steps are also almost identical,
181 suggesting using 5000 particles was adequate for our global simulation.

182   To determine an adequate time duration for each HYSPLIT simulation, we compared
183   footprints for observations with enhanced CFC-11 mole fractions versus those with relatively low
184   mole fractions for observations made at different altitudes and latitudes from ATom-2. Our results
185   show that, for observations in all altitude and latitude bins, those with enhanced CFC-11 mole
186   fractions always had higher sensitivity to upwind populated regions in the first 20 days (Fig. S2);
187   after that, the overall sensitivity was relatively small and constant, likely due to evenly distributed
188   particles throughout the troposphere beyond 20 days. This result suggests running HYSPLIT for
189   more than 20 days was likely sufficient for capturing the major emission influence on atmospheric
190   CFC-11 mole fraction observations made over the remote atmosphere. In the analysis presented
191   here, sensitivities were derived with HYSPLIT-GDAS0.5^o by tracking 5000 particles back in time
192   for 30 days.
193
194   **2.2.3. Estimation of background mole fractions**
195   As described above, emissions are derived from measured mole fraction enhancements
196   above background values. For each observation, the background mole fraction was estimated
197   based on the 5000 HYSPLIT-GDAS0.5^o back-trajectories and a 4D background mole fraction
198   field. We tested various approaches for constructing this 4D CFC-11 mole fraction field (see
199   supplementary information; Figs. S3 and S4). Here, we only describe the final choice selected for
200   the inversion analysis. The final empirical 4D CFC-11 mole fraction field was constructed based
201   on NOAA observations by propagating a subset of measured mole fractions of CFC-11 from the
202   NOAA's global surface and ongoing airborne flask-air sampling programs back in time along the
203   5000 back-trajectories for 10 days. Observations were included in the background estimate if the
204   associated mole fraction was lower than the 70 – 80th percentile of all results in each 30° in latitude
205   x 3 km in altitude box during the HIPPO period and the 40 – 50th percentile of all results in each
206   box during the ATom period. These thresholds were chosen to ensure that the inversely derived
207   global emissions in both periods were consistent with those derived from a global 3 box model
208   and a best estimate of atmospheric CFC-11 lifetime (Montzka et al., 2021). Although the inversely
209   derived global emission total was sensitive to the choice of the background threshold, the relative
210   regional emission distribution or the fraction of regional emissions to the global emission was
211   not. By propagating this subset of observations back in time, it provided a 4D field of CFC-11
212   background mole fractions that we then averaged every 5° latitude $\times$ 20° longitude $\times$ 2 km
213   altitude every month. This 4D empirical background did not account for the strong stratospheric
214   influence on CFC-11 mole fractions at high altitudes (8 - 10 km) in the polar regions (> 60°N or >
215   60°S). Thus, we further scaled the CFC-11 mole fractions in these areas using the vertical gradients
216   simulated by the Whole Atmosphere Community Climate Model (WACCM) (Davis et al., 2020;
217   Marsh et al., 2013; Montzka et al., 2021; Ray et al., 2020).
218   From this 4D background mole fraction field, we sampled 5000 mole fraction estimates at
219   the locations of the 5000 back-trajectories at the end of the 30 days and then averaged these 5000
220   mole fraction estimates to obtain one background mole fraction for each observation. We
221   examined the particle locations at the end of the 30 days using observations collected at 0 - 8 km
222   from ATom-2. For the majority of these observations, 80 % - 100 % of particles were located
223   between 0 and 10 km at the end of the 30 days in the HYSPLIT back-trajectory runs. For particles
224   that exited from the top at 10 km before 30 days, we sampled the mole fractions at 10 km when
225   they exited the background mole fraction field.
226
227   **2.2.4. Prior emissions**

228   We constructed 11 different prior emission fields for inversion analyses in both the HIPPO
229   and ATom periods (Fig. 2). The first prior emission field or "a priori" was constructed with an
230   assumed global CFC-11 emission of 67 Gg yr^{-1}. This global total was distributed around the globe
231   in a 1° x 1° resolution based on a 1° x 1° gridded population density product from the Gridded
232   Population of the World (GPW) v4 dataset (https://sedac.ciesin.columbia.edu/data/collection/gpw-
233   v4). The only exception is over the US, where we used the 1° x 1° gridded annual emissions
234   derived from Hu et al. (2017) for 2014. The second a priori emission has the same distribution as
235   the first a priori, except the total emission magnitude was reduced by 40% across the globe, such
236   that the global CFC-11 emission in this scenario is 40 Gg yr^{-1}. The other 9 prior emission fields
237   were constructed as the first a priori, but with an additional 20 Gg yr^{-1} of emission imposed over
238   North America, South America, Africa, Europe, Australia, boreal Asia, temperate eastern Asia,
239   temperate western Asia, and tropical Asia. The 20 Gg yr^{-1} of emissions was added to those regions
240   by a constant emission rate in pmol m^{-2} s^{-1} across the grid cells having non-zero emissions in the
241   first prior emissions. The regions specified as North America (NA), South America (SA), Africa
242   (Af), Europe (Eu), Australia (Au), boreal Asia (BA), temperate eastern Asia (TEA), temperate
243   western Asia (TWA), and tropical Asia (TA) are shown in Fig. 3. We named the 11 different prior
244   emission fields as "population_GlobalEmission" or "population_GlobalEmission_region" (Fig.
245   2), where "population" represents their distribution; "GlobalEmission" represents the global
246   emission in Gg yr^{-1} in each prior; "region" represents the location where the additional 20 Gg yr^{-1}
247   of emission was added. For example, "population_87_TEA" indicates a priori with a global CFC-
248   11 emission of 87 Gg yr^{-1} and a distribution similar to population density; compared to the first a
249   priori, this a priori had additional 20 Gg yr^{-1} emissions imposed over TEA.
250   We assume an exponential decaying covariance function in the errors of prior emissions
251   (Hu et al., 2017).

$$252 \quad Q = \sigma_q^2 \begin{bmatrix} 1 & \exp\left(-\frac{h_{s,1,2}}{\tau_l}\right)\exp\left(-\frac{h_{t,1,2}}{\tau_t}\right) & \cdots & \exp\left(-\frac{h_{s,1,m}}{\tau_l}\right)\exp\left(-\frac{h_{t,1,m}}{\tau_t}\right) \\ \exp\left(-\frac{h_{s,2,1}}{\tau_l}\right)\exp\left(-\frac{h_{t,2,1}}{\tau_t}\right) & 1 & \cdots & \exp\left(-\frac{h_{s,2,m}}{\tau_l}\right)\exp\left(-\frac{h_{t,2,m}}{\tau_t}\right) \\ \vdots & \vdots & \vdots & \vdots \\ \exp\left(-\frac{h_{s,m,1}}{\tau_l}\right)\exp\left(-\frac{h_{t,m,1}}{\tau_t}\right) & \exp\left(-\frac{h_{s,m,2}}{\tau_l}\right)\exp\left(-\frac{h_{t,m,2}}{\tau_t}\right) & \cdots & 1 \end{bmatrix} \quad (2)$$

253   where σ_q represents the 1 sigma error on a relative scale in the prior emission; τ_l and τ_t denote the
254   spatial and temporal correlation lengths of prior emission error (the 95% correlation scales are
255   approximately 3 τ_l and 3 τ_t). h_t and h_s are temporal intervals and spatial distance between state
256   vectors; and m stands for the number of state vectors. h_t and h_s can be calculated based on air
257   sampling times and locations. σ_q, τ_l, and τ_t are prior emission-dependent and were estimated by the
258   maximum likelihood estimation. σ_q was estimated in a range of 200 – 340 % given the 9 different
259   prior emission fields. The spatial and temporal correlation lengths were estimated as 2.5 km and
260   58 days. Prior uncertainty in regional emissions were then calculated by considering spatial and
261   temporal correlations in space and time. The calculated 1-σ uncertainty for the 9 different priors
262   is 20 – 60% on a global scale and 20 – 120 % on a regional scale.

263

264 **2.2.5. Inversion ensembles**

265   We constructed 23 inversion ensembles for deriving global and regional emissions in the
266 HIPPO and ATom periods. These 23 inversion ensembles included 20 different prior emission
267 change scenarios between the HIPPO and ATom periods, two background CFC-11 mole fraction
268 fields, and two sets of observations ("flask only" and "flask + in situ") (Table S1). The 20 prior
269 emission change scenarios assumed: (scenario 1) no increase of global CFC-11 emissions between
270 the HIPPO and ATom periods (inversion ensemble IDs #1 - #5 in Table S1); (scenario 2) a 20 Gg
271 yr^{-1} increase of CFC-11 emissions between the HIPPO and ATom periods, with the increase being
272 restricted to one of the following regions, respectively: North America, South America, Africa,
273 Europe, Australia, boreal Asia, temperate eastern Asia, temperate western Asia, and tropical Asia
274 (inversion ensemble IDs #6 - #14 in Table S1); and (scenario 3) a 20 Gg yr^{-1} decrease of CFC-11
275 emissions between the HIPPO and ATom periods, with the decrease being restricted to one of the
276 following regions, respectively: North America, South America, Africa, Europe, Australia, boreal
277 Asia, temperate eastern Asia, temperate western Asia, and tropical Asia (inversion ensemble IDs
278 #15 - #23 in Table S1).

279   In our global inversions, we solved for monthly 1º x 1º emissions and their posterior
280 covariances at 1º x 1º resolution. Because the uncertainty associated with the 1º x 1º emissions is
281 large, we aggregated emissions and their posterior covariances into regional, continental, and
282 global scales for the HIPPO and ATom periods, considering the cross correlation in errors among
283 grid cells and across times for each inversion (Hu et al., 2017). In this study, we report the mean
284 (μ_i) and 2 standard deviations ($2\sigma_i$) of posterior estimates for each inversion scenario, where *i*
285 denotes the inversion ID in Table S1. In the final results summarized in Table 1, we report two
286 types of uncertainties. The first uncertainty is calculated as the 2.5[th] – 97.5[th] percentile range of
287 the mean emissions (μ_i) derived from the 23 inversions, and are considered our "best estimates"
288 of emissions. Uncertainties were also calculated considering the uncertainty ($2\sigma_i$) associated with
289 each inversion. The lower bound of this second uncertainty was calculated as the 2.5[th] percentile
290 of $[\mu_1 - 2\sigma_1, \mu_2 - 2\sigma_2, \dots, \mu_{23} - 2\sigma_{23}]$ and the upper bound was calculated as the 97.5[th] percentile
291 of $[\mu_1 + 2\sigma_1, \mu_2 + 2\sigma_2, \dots, \mu_{23} + 2\sigma_{23}]$.

292

293 **3. Results and Discussion**

294 **3.1. Increase of CFC-11 emissions between the HIPPO and ATom periods observed in remote**
295 **atmospheric observations**

296   The global increase of CFC-11 emissions between 2012 and 2017 was previously derived
297 from the slow-down in the decline of atmospheric CFC-11 mole fractions observed at Earth's
298 surface (Montzka et al., 2021; Montzka et al., 2018) and is also shown in Fig. 4 here. Besides at
299 Earth's surface, a similar magnitude of this slow-down in atmospheric CFC-11 mole fraction
300 decline is also apparent throughout the free troposphere in the aircraft profiles obtained during the
301 HIPPO and ATom campaigns, each of which involved sampling deployments spread over
302 approximately two years (Fig. 4). Here, we calculated the CFC-11 growth rates averaged in each
303 30º in latitude × 2 km in altitude box during HIPPO campaigns and during ATom campaigns
304 separately for samples collected above the Pacific Ocean basin. During HIPPO, we calculated the
305 average mole fraction differences in each 30º in latitude × 2 km in altitude box between HIPPO-
306 3 (3/2010 – 4/2010) and HIPPO-4 (6/2011 – 7/2011) and normalized by their time interval to
307 obtain annual growth rates, whereas we calculated annual growth rates during ATom using the

7

308   ATom-1 (7/2016 – 8/2016) and ATom-4 (4/2018 – 5/2018) data. The reason to choose HIPPO-3,
309   HIPPO-4, ATom-1, and ATom-4 for this calculation is to ensure annual growth rates were
310   calculated from data collected in similar seasons, so that the impact of seasonal variations in
311   atmospheric CFC-11 mole fractions on the calculated annual growth rates was minimized (Fig.
312   S5). Results suggest a median growth rate of -2.5 ppt yr^{-1} between 60°S and 90°N in the
313   troposphere during the HIPPO period and a median growth rate of -0.7 ppt yr^{-1} during the ATom
314   period (Fig. 4), indicating a significant increase of CFC-11 growth rates in the troposphere between
315   the HIPPO and ATom periods. The impact of the atmospheric CFC-11 seasonal cycle measured
316   at the surface on the calculated changes of annual growth rates between both periods is about $\pm$0.1
317   ppt. Besides the seasonal cycle of atmospheric CFC-11 mole fractions, the Quasi-Biennial
318   Oscillation (QBO) can also influence atmospheric trace gas mole fractions in the troposphere (Ray
319   et al., 2020) and thus their growth rates. However, this influence was smaller than the increase of
320   the annual growth rates between the HIPPO and ATom periods, as quantified in Montzka et al.
321   (2021).
322   After subtracting background CFC-11 mole fractions from the selected global CFC-11
323   observations, enhancements approaching 3 ppt were found in air above the Pacific Ocean basin
324   during both sampling periods by all measurements methods (onboard the HIPPO and ATom
325   aircraft surveys, from the global weekly flask sampling, and from the selected daily to "every other
326   day" in situ sampling) (Fig. 5). Relatively larger enhancements were more frequently measured
327   during the ATom period than during the HIPPO period (Fig. 5). However, the average increase in
328   enhancements of the atmospheric CFC-11 mole fractions measured during ATom were 0.2 – 0.3
329   ppt higher than observed during the HIPPO campaign (Fig. 5). The 0.2 – 0.3 ppt increase in the
330   atmospheric CFC-11 enhancements was also independently measured by the global weekly flask
331   sampling, and in situ sampling networks over the Pacific Ocean basin (Fig. 5). Results
332   from HIPPO and ATom suggest that increased mole fraction enhancements over the Pacific Ocean
333   basin existed primarily between 0 and 60 °N (Fig. 5), where the lower and middle tropospheric air
334   mainly contains emissive signals from Eurasia, western North America, and tropical America (Fig.
335   S6). Furthermore, during ATom, CFC-11 enhancements measured in the Pacific Ocean basin were
336   larger than those measured in the Atlantic Ocean basin (Fig. 5), suggesting regions immediately
337   upwind of the Pacific Ocean were emitting more CFC-11 than regions upwind of the Atlantic
338   Ocean (Fig. 1b) during the ATom period.
339
340   **3.2. Regional emissions derived from HIPPO and ATom global inversions**
341   **3.2.1. The base scenarios with only flask-air measurements**
342   To quantitatively understand what measured atmospheric CFC-11 variability implies for
343   global and regional CFC-11 emissions, we conducted Bayesian inversions as described in Section
344   2. We first only used the flask-air measurements made by the two GCMS instruments. These
345   measurements include samples collected during HIPPO and ATom, the global weekly flask-air
346   sampling program, and the regular aircraft flask-air sampling program located primarily over
347   North America. The inversions derived from these flask-air measurements are referred to here as
348   "flask-only inversions". In this first base scenario, we used the same prior emission with a global
349   CFC-11 emission of 67 Gg yr^{-1} ("population_67" shown in Fig. 2) for both HIPPO and ATom
350   periods (Table S1). The global emissions derived from this scenario (67 $\pm$ 7 Gg yr^{-1} and 87 $\pm$
351   9 Gg yr^{-1} for the HIPPO and ATom periods) were based on background estimates that were
352   calibrated against the global 3-box model results, such that the global CFC-11 emissions derived

353 from the grid-scale inversions were consistent with those from the global 3-box model with an
354 atmospheric lifetime of 52 years reported by Montzka et al. (2021).
355   An inverse analysis of the flask data obtained during the HIPPO and ATom periods suggest
356 changes in the total magnitude and distribution of CFC-11 emissions from 2010 to
357 2018. Significant emission increases were derived for Asia by an amount that suggests it was
358 primarily responsible for the global CFC-11 emission increase from 2010 to 2018. During the
359 HIPPO period (November 2009 – September 2011), Asia emitted 35 ($\pm$5) Gg yr^{-1} of CFC-11,
360 accounting for 50% of global CFC-11 emissions, whereas Asian annual CFC-11 emissions
361 increased to 51 ($\pm$8) Gg yr^{-1} during the ATom period in August 2016 – May 2018, equal to 60%
362 of the global CFC-11 emission at that time. Results from this scenario yield an increase of CFC-
363 11 emission from Asia during these two periods of 16 ($\pm$10) Gg yr^{-1}, which accounted for 80 -
364 90 % of global CFC-11 emission increases during these specific years (19 $\pm$12) (Fig. 6), as derived
365 from this scenario.
366   Our inversion results also suggest that the Asian CFC-11 emissions and emission increases
367 were primarily contributed by the temperate eastern Asia, temperate western Asia, and tropical
368 Asia in approximately equal amounts (Fig. 6). Correlations (as r^2) or covariations in the posterior
369 emissions among these three Asian subregions were less than 0.1, suggesting the inversion was
370 able to separate regional total emissions from these three subregions, although the derived
371 analytical uncertainties associated with emissions at the subregional level are overlapping (Fig. 6).
372   Emissions derived for North America, South America, Africa, and Europe were 5 – 15 Gg
373 yr^{-1} for each region in both the HIPPO and ATom periods. Emissions derived for Australia were
374 less than 1 Gg yr^{-1}. Changes of CFC-11 emissions between both periods derived for all seven of
375 these continents were smaller than their associated uncertainties in this scenario.
376   With "flask-only" observations, we also tested the sensitivity of posterior regional
377 emissions to the prior emission magnitude. Here, we considered the second "population-density"
378 prior with a substantially lower global total CFC-11 emission of 40 Gg yr^{-1} for both periods
379 ("population_40") (Table S1). Derived regional emissions from this second scenario were
380 consistent with results discussed in the first scenario in both the distribution and total magnitude
381 of posterior emissions.
382   To assess how much constraint the selected atmospheric observations added to regional
383 emission estimates, we calculated the uncertainty reduction between the prior and posterior
384 emission uncertainties. Note that the uncertainty reduction is generally correlated with the
385 sensitivity of atmospheric observations to surface emissions (or footprint) and is dependent on how
386 good the prior emission is. As expected, the uncertainty reduction is indeed the largest (50 – 80%)
387 over North America and Asia (Table S2; Fig. 6), where our observations have the strongest
388 sensitivity, and the smallest over South America, Africa, and Australia (3 – 50%) (Fig. 6; Table
389 S2), where our observations have the lowest sensitivity (Fig. 1).
390
391 **3.2.2. Inversions using more observations, different prior assumptions, and an alternative**
392 **background mole fraction field**
393   To increase the observational constraints in the global CFC-11 inversion, we then included
394 additional observations from the in situ CFC-11 measurements (Fig. 1; Inversion ID = 3 – 4 in
395 Table S1). The derived posterior emissions with this expanded observational dataset (and with the
396 same population-based priors and background estimates) show slightly higher global emissions,
397 especially from tropical Asia, during the ATom period (Fig. 7). Besides inclusion of additional
398 observations, we also considered an alternative background estimate (background 2) that was

399   calibrated to the global CFC-11 emission estimates with alternative atmospheric lifetimes (54 and
400   56 years) (Montzka et al., 2021) (Inversion ID = 5 in Table S1). As expected, the derived global
401   and regional emissions were lower with a background calibrated to a longer atmospheric lifetime.
402   However, the derived regional contributions to the global CFC-11 emissions and emission changes
403   between the HIPPO and ATom periods were consistent with results considering a shorter lifetime
404   (Fig. 7).
405   Results discussed so far are based on prior emissions that do not change between the
406   HIPPO and ATom periods for all regions considered. The remaining questions are: 1) are the
407   resulting near-zero emission changes over North America, South America, Africa, Europe, and
408   Australia due to the influence from prior assumption (zero emission changes in the prior) or are
409   they the result of observational constraints? and 2) to what degree are derived Asian emissions and
410   emission changes dependent on assumptions of prior emission changes? To address these
411   questions, we constructed 18 additional scenarios (as part of the 23 scenarios described in Section
412   2.2.5) that assumed 20 Gg yr^{-1} CFC-11 emission increases in the prior emissions between the
413   HIPPO and ATom (Inversion ID = 6 - 14 in Table S1) or 20 Gg yr^{-1} CFC-11 emission decreases
414   between the HIPPO and ATom periods (Inversion ID = 15 – 23 in Table S1). In the first 9 cases,
415   we considered the same population-based prior with a global CFC-11 emission of 67 Gg yr^{-1} during
416   the HIPPO period (prior = "population_67"), whereas during the ATom period, we assumed there
417   was an increase of 20 Gg yr^{-1} of CFC-11 emissions over individual continents (North America,
418   South America, Africa, Europe, Australia) or individual Asian subregions (boreal Asia, temperate
419   eastern Asia, temperate western Asia, and tropical Asia) (prior = "population_87_region"). In the
420   latter 9 cases, we considered opposite scenarios, where we assumed 67 Gg yr^{-1} of emissions during
421   the ATom period (prior = "population_67") and 87 Gg yr^{-1} of emissions during the HIPPO period
422   (prior = "population_87_region"), so that emissions over individual continents or individual Asian
423   subregions had a 20 Gg yr^{-1} decrease between both periods (Fig. 8). Note that, given it is known
424   there was a global increase of CFC-11 emissions from 2010 to 2018 (Montzka et al., 2021;
425   Montzka et al., 2018) and 60 ± 40 % of this global increase was from eastern mainland China (Park
426   et al., 2021; Rigby et al., 2019), many of the assumed 18 prior emission change cases were quite
427   unrealistic. However, such extreme cases helped for estimating uncertainties that truly reflect the
428   capability of the selected atmospheric measurements for constraining continental and regional
429   emissions and their change through time. In all of the 18 extreme cases, regional emissions and
430   emission changes derived for the northern hemispheric lands, i.e. Asia, North America, Europe,
431   were consistent (Fig. 8). Derived regional emissions and emission changes for the southern
432   hemispheric lands, such as South America, Africa, Australia, however, show a strong dependence
433   on prior assumptions, especially during the ATom period (Fig. 8). The strong dependence of
434   inversion-derived emissions over the southern hemispheric lands were due to large sampling gaps
435   and small sensitivity to emissions from these regions (Fig. 1).
436   Summarizing emissions derived from all 23 inversion ensembles (Table 1; Figs. 6 - 8), our
437   results suggest the relatively remote observations provide important constraints on regional
438   emissions from North America, Asia, and Europe, as the derived ranges of posterior emissions
439   were smaller than the ranges of prior emissions considered for these regions (Figs. 6 - 8). The
440   only continent that shows a statistically significant increase of CFC-11 emissions is Asia, where
441   the best estimate of these 23 cases suggests an increase of 24 (18 – 28) Gg yr^{-1} of CFC-11 emissions
442   (the 2.5[th] – 97.5[th] percentile range) (Table 1), accounting for 86 (59 – 115) % of the global CFC-
443   11 emission increases between the HIPPO and ATom periods. All the best estimates from the 23
444   inversion ensembles suggest CFC-11 emission increases not only from temperate eastern Asia, but

445   also from temperate western Asia and tropical Asia. However, if we consider the entire range of
446   uncertainties (the range of best estimates and $2\sigma_i$ errors from each inversion; Table 1), the derived
447   emission increases were statistically insignificant at the subregion level (i.e., temperate eastern
448   Asia, temperate western Asia, and tropical Asia).

449   Our results also suggest inverse modeling of the relatively remote observations we
450   considered here provided only weak constraints on emissions from the southern hemispheric
451   continents, i.e., South America, Africa, and Australia. Although we cannot eliminate the
452   possibility of some increase in CFC-11 emissions from these southern hemispheric regions based
453   on atmospheric inversion analyses alone, they did not account for the majority of the emission
454   increase. This is because during 2010 – 2018, when the global CFC-11 emissions increased, so
455   did the north-to-south mole fraction difference between the hemispheres (Montzka et al., 2021),
456   which indicates the emission increase occurred predominantly in the northern hemisphere.

457

3.2.3. Comparison of regional emission estimates from other top-down analyses

459   Our regional emission estimates of CFC-11 from the global atmospheric CFC-11
460   measurements made far away from the emissive regions are in a broad agreement with those
461   estimated from atmospheric observations made closely downwind of the emissive regions (Table
462   2), which included the analyses of atmospheric CFC-11 enhancements observed closely downwind
463   of emissive regions that were one-two orders of magnitude larger than those used in the present
464   inversion analysis (Park et al., 2021; Rigby et al., 2019; Hu et al., 2017; Fraser et al., 2020).
465   Emissions estimated for eastern mainland China using measurements made in South Korea were
466   5 – 13 Gg yr^{-1} during 2010 – 2011 and 12 – 20 Gg yr^{-1} during 2016 - 2017, considering the full
467   range of estimates from multiple inversion systems with different transport simulations (Park et
468   al., 2021). CFC-11 emission estimates for eastern China based on measurements made in Taiwan
469   were 14 – 23 Gg yr^{-1} during 2014 – 2018 (Adcock et al., 2020). In the current analysis, we
470   estimated CFC-11 emissions from temperate eastern Asia were 5 – 16 Gg yr^{-1} during Nov 2009 –
471   Sep 2011 and 9 – 22 Gg yr^{-1} during August 2016 – May 2018, which agree well with the published
472   analyses over eastern China, although our definition of temperate eastern Asia is slightly different
473   from the regions defined in Rigby et al. (2019), Adcock et al. (2020) and Park et al. (2021).

474   Previously, we estimated the US emissions of CFC-11 between 2008 and 2014 with more
475   extensive atmospheric measurements made from towers and aircraft sites from all vertical levels
476   over North America (Hu et al., 2017). In this analysis, we only used a subset of observations (only
477   aircraft observations above 1 km above ground) and a coarser resolution of transport models in the
478   global inversion. While the North American CFC-11 emissions derived here are likely not as
479   accurate, they did agree within uncertainties with our previous US estimates (Table 2).

480   Furthermore, CFC-11 emissions derived for Australia are also comparable with estimates
481   reported by Fraser et al. (2020) using measurements made in Australia (Table 2). Both suggest
482   CFC-11 emissions from Australia were less than 1 Gg yr^{-1} between 2009 and 2018, and
483   contributions from Australia to global CFC-11 emissions and emission changes were very small.

484   Besides temperate eastern Asia, North America, and Australia, we also compared our
485   derived European CFC-11 emissions for Nov 2009 – Sep 2011 with the value reported by Keller
486   et al. (2011) for western Europe in 2009. Our best estimate of 4.2 (2.9 - 5.4) Gg yr^{-1} for all of
487   Europe was about twice as large as reported by Keller et al. (2011) for the western Europe, which
488   only accounted for 40% of the area we considered for all of Europe. If aggregating emissions from
489   only grid cells considered in Keller et al. (2011), the aggregated total emissions would be similar

11

490   to the value reported by Keller et al. (2011), although both studies focused on two different time
491   periods (Table 2).

492   Other than the regions mentioned above, previous emission estimates for the rest of the
493   world are quite limited. Only one study quantified CFC-11 emissions from the northern and central
494   areas of India in June 2016, reporting emissions of $\sim 1 - 3$ Gg yr^{-1} (Say et al., 2019). It is hard to
495   make a fair comparison with our analysis, given its short analysis period and a much smaller area
496   than our defined temperate western Asian region (Fig. 4). However, there is observational
497   evidence indicating likely strong regional emissions and a regional emission increase over
498   temperate western Asia between 2012 – 2017. This was shown as substantially enhanced CFC-11
499   mole fractions observed in temperate western Asia for flask measurements made during 2012 –
500   2018 (Simpson et al., 2019) and the slow-down of atmospheric CFC-11 decline retrieved from
501   satellite remote sensing measurements (Chen et al, 2020). Furthermore, in situ measurements
502   made in tropical Asia in 2017 (Lin et al., 2019) also indicate likely strong regional emissions of
503   CFC-11 over this area.

504

505   **4. Conclusions**

506   We used global atmospheric CFC-11 measurements primarily made over the Pacific and
507   Atlantic Ocean basins and in the free troposphere over North America to quantify changes in
508   continental-scale emissions between November 2009 - September 2011 and August 2016 – May
509   2018. These two periods covered the times when global CFC-11 emissions were at their minimum
510   and maximum, respectively, in recent years, at least before the sharp decline noted after 2018
511   (Montzka et al., 2021). Atmospheric CFC-11 measurements made during both the HIPPO and
512   ATom campaigns confirm that the slow-down of atmospheric CFC-11 mole fraction decline
513   between 2009 and 2018 was present throughout the troposphere. The ATom campaign data further
514   display larger atmospheric CFC-11 enhancements in flights, particularly over the Pacific Ocean
515   basin as compared to the Atlantic Ocean basin, suggesting larger emissions in regions immediately
516   upwind of the Pacific Ocean than the Atlantic Ocean during 2016-2018.

517   Inverse modeling of these global atmospheric CFC-11 measurements suggests three Asian
518   regions were primarily responsible for the global CFC-11 emission changes from 2009-11 to 2016-
519   18 in all of the 23 inversion ensembles, including various extreme initial assumptions of regional
520   CFC-11 emission changes ($\pm$ 20 Gg yr^{-1}) between both periods. Our results suggest that, during
521   November 2009 – September 2011, Asia emitted 24 (14 – 40) Gg yr^{-1} of CFC-11, accounting for
522   43 (37 – 52) % of the global emission (Table 1), whereas the Asian CFC-11 emissions increase to
523   48 (38 – 65) Gg yr^{-1} or 57 (49 - 62) % of the global emission during August 2016 – May 2018
524   (Table 1). In both periods, substantial CFC-11 emissions were derived for temperate eastern Asia,
525   temperate western Asia, and tropical Asia. Besides eastern mainland China, our results suggest
526   there could be increases of CFC-11 emissions from temperate western Asia and tropical Asia from
527   2010 to 2018, considering the range of best estimates from the 23 inversion ensembles. In contrast
528   to Asia, other continents accounted for relatively smaller fractions of global CFC-11 emissions in
529   both periods. For continents in the Southern Hemisphere, our inversion analyses only provide weak
530   constraints on the CFC-11 emission changes between 2012 and 2018. However, significant
531   increases in CFC-11 emissions from these regions are unlikely, provided the observed concurrent
532   increase of the north-to-south difference in CFC-11 surface mole fractions.

533

534   **Acknowledgement**

541

542 **Code/Data availability:** NOAA atmospheric observations are available at the NOAA/GML
543 website (https://gml.noaa.gov/hats/). Data collected from ATom are available via
544 https://espo.nasa.gov/atom/content/ATom and https://doi.org/10.3334/ORNLDAAC/1581. Data
545 collected from HIPPO are available via
546 https://www.nsf.gov/news/news_summ.jsp?cntn_id=127003. Inversion-derived continental
547 fluxes were tabulated and described in this paper. All analysis tools and computing code used in
548 this analysis will be available by contacting LH (lei.hu@noaa.gov).

549

550 **Author contributions**
551 LH and SAM designed the analysis; LH conducted inversions and wrote the paper; SAM led the
552 NOAA global flask measurements, HIPPO and ATom GCMS measurements, and provided
553 substantial input on the analyses and edits of this paper; FM and EH collected HIPPO and ATom
554 flask-air samples; GD led the CATS measurements and prepared CATS data for this analysis;
555 MCS made the NOAA flask measurements; LH and KT computed HYSPLIT footprints; RWP
556 conducted the WACCM simulations and provided the model results; KM conducted NOAA
557 aircraft data QA/QC; CW led the NOAA aircraft sampling network; IV led the Persus GCMS flask
558 measurements; DN helped with data QA/QC for CFC-11 flask measurements; BH led the
559 calibration for NOAA measurements; SW led the HIPPO and ATom campaigns; all authors
560 contributed to the editing of this paper.

561

562 **Competing interests:** the authors declare no competing interests.

563

564 **References**

565 Adcock, K. E., Ashfold, M. J., Chou, C. C. K., Gooch, L. J., Mohd Hanif, N., Laube, J. C., Oram,
566 D. E., Ou-Yang, C.-F., Panagi, M., Sturges, W. T., and Reeves, C. E.: Investigation of East Asian
567 Emissions of CFC-11 Using atmospheric observations in Taiwan, Environmental Science &
568 Technology, 54, 3814-3822, 10.1021/acs.est.9b06433, 2020.

569 Bourgeois, I., Peischl, J., Thompson, C. R., Aikin, K. C., Campos, T., Clark, H., Commane, R.,
570 Daube, B., Diskin, G. W., Elkins, J. W., Gao, R. S., Gaudel, A., Hintsa, E. J., Johnson, B. J., Kivi,
571 R., McKain, K., Moore, F. L., Parrish, D. D., Querel, R., Ray, E., Sánchez, R., Sweeney, C.,
572 Tarasick, D. W., Thompson, A. M., Thouret, V., Witte, J. C., Wofsy, S. C., and Ryerson, T. B.:
573 Global-scale distribution of ozone in the remote troposphere from the ATom and HIPPO airborne
574 field missions, Atmos. Chem. Phys., 20, 10611-10635, 10.5194/acp-20-10611-2020, 2020.

575 Chen, X., Huang, X., and Strow, L. L.: Near-Global CFC-11 trends as observed by Atmospheric
576 Infrared Sounder From 2003 to 2018, Journal of Geophysical Research: Atmospheres, 125,
577 e2020JD033051, https://doi.org/10.1029/2020JD033051, 2020.

578 Davis, N. A., Davis, S. M., Portmann, R. W., Ray, E., Rosenlof, K. H., and Yu, P.: A
579 comprehensive assessment of tropical stratospheric upwelling in the specified dynamics
580 Community Earth System Model 1.2.2 – Whole Atmosphere Community Climate Model (CESM
581 (WACCM)), Geosci. Model Dev., 13, 717-734, 10.5194/gmd-13-717-2020, 2020.

582 Dhomse, S. S., Feng, W., Montzka, S. A., Hossaini, R., Keeble, J., Pyle, J. A., Daniel, J. S., and
583 Chipperfield, M. P.: Delay in recovery of the Antarctic ozone hole from unexpected CFC-11
584 emissions, Nature Communications, 10, 5781, 10.1038/s41467-019-13717-x, 2019.

585 Engel, A., Rigby, M., Burkholder, J. B., Fernandez, R. P., Froidevaux, L., Hall, B. D., Hossaini,
586 R., Saito, T., Vollmer, M. K., and Yao, B.: Update on Ozone-Depleting Substances (ODSs) and
587 Other Gases of Interest to the Montreal Protocol, Chapter 1 in Scientific Assessment of Ozone
588 Depletion: 2018, World Meteorological Organization, Geneva, Switzerland, 2018.

589 Fraser, P. J., Dunse, B. L., Krummel, P. B., Steele, L. P., Derek, N., Mitrevski, B., Allison, C. E.,
590 Loh, Z., Manning, A. J., Redington, A., and Rigby, M.: Australian chlorofluorocarbon (CFC)
591 emissions: 1960–2017, Environmental Chemistry, 17, 525-544, https://doi.org/10.1071/EN19322,
592 2020.

593 Hu, L., Montzka, S. A., Lehman, S. J., Godwin, D. S., Miller, B. R., Andrews, A. E., Thoning, K.,
594 Miller, J. B., Sweeney, C., Siso, C., Elkins, J. W., Hall, B. D., Mondeel, D. J., Nance, D., Nehrkorn,
595 T., Mountain, M., Fischer, M. L., Biraud, S. C., Chen, H., and Tans, P. P.: Considerable
596 contribution of the Montreal Protocol to declining greenhouse gas emissions from the United
597 States, Geophysical Research Letters, 44, 2017GL074388, 10.1002/2017GL074388, 2017.

598 Hu, L., Montzka, S. A., Miller, B. R., Andrews, A. E., Miller, J. B., Lehman, S. J., Sweeney, C.,
599 Miller, S. M., Thoning, K., Siso, C., Atlas, E. L., Blake, D. R., de Gouw, J., Gilman, J. B., Dutton,
600 G., Elkins, J. W., Hall, B., Chen, H., Fischer, M. L., Mountain, M. E., Nehrkorn, T., Biraud, S. C.,
601 Moore, F. L., and Tans, P.: Continued emissions of carbon tetrachloride from the United States
602 nearly two decades after its phaseout for dispersive uses, Proceedings of the National Academy of
603 Sciences, 113, 2880-2885, 10.1073/pnas.1522284113, 2016.

604 Hu, L., Montzka, S. A., Miller, J. B., Andrews, A. E., Lehman, S. J., Miller, B. R., Thoning, K.,
605 Sweeney, C., Chen, H., Godwin, D. S., Masarie, K., Bruhwiler, L., Fischer, M. L., Biraud, S. C.,
606 Torn, M. S., Mountain, M., Nehrkorn, T., Eluszkiewicz, J., Miller, S., Draxler, R. R., Stein, A. F.,
607 Hall, B. D., Elkins, J. W., and Tans, P. P.: U.S. emissions of HFC-134a derived for 2008–2012
608 from an extensive flask-air sampling network, Journal of Geophysical Research: Atmospheres,
609 2014JD022617, 10.1002/2014JD022617, 2015.

610 Keeble, J., Abraham, N. L., Archibald, A. T., Chipperfield, M. P., Dhomse, S., Griffiths, P. T., and
611 Pyle, J. A.: Modelling the potential impacts of the recent, unexpected increase in CFC-11
612 emissions on total column ozone recovery, Atmos. Chem. Phys., 20, 7153-7166, 10.5194/acp-20-
613 7153-2020, 2020.

614 Keller, C. A., Brunner, D., Henne, S., Vollmer, M. K., O'Doherty, S., and Reimann, S.: Evidence
615 for under-reported western European emissions of the potent greenhouse gas HFC-23,
616 Geophysical Research Letters, 38, L15808, 10.1029/2011gl047976, 2011.

617 Lin, Y., Gong, D., Lv, S., Ding, Y., Wu, G., Wang, H., Li, Y., Wang, Y., Zhou, L., and Wang, B.:
618 Observations of High Levels of Ozone-Depleting CFC-11 at a Remote Mountain-Top Site in

619 Southern China, Environmental Science & Technology Letters, 6, 114-118,
620 10.1021/acs.estlett.9b00022, 2019.

621 Marsh, D. R., Mills, M. J., Kinnison, D. E., Lamarque, J.-F., Calvo, N., and Polvani, L. M.: Climate
622 Change from 1850 to 2005 Simulated in CESM1(WACCM), Journal of Climate, 26, 7372-7391,
623 10.1175/jcli-d-12-00558.1, 2013.

624 Michalak, A. M., Hirsch, A., Bruhwiler, L., Gurney, K. R., Peters, W., and Tans, P. P.: Maximum
625 likelihood estimation of covariance parameters for Bayesian atmospheric trace gas surface flux
626 inversions, Journal of Geophysical Research: Atmospheres, 110, D24107, 10.1029/2005jd005970,
627 2005.

628 Montzka, S. A., Dutton, G. S., Yu, P., Ray, E., Portmann, R. W., Daniel, J. S., Kuijpers, L., Hall,
629 B. D., Mondeel, D., Siso, C., Nance, J. D., Rigby, M., Manning, A. J., Hu, L., Moore, F., Miller,
630 B. R., and Elkins, J. W.: An unexpected and persistent increase in global emissions of ozone-
631 depleting CFC-11, Nature, 557, 413-417, 10.1038/s41586-018-0106-2, 2018.

632 Montzka, S. A., Dutton, G. S., Portmann, R. W., Chipperfield, M. P., Davis, S., Feng, W.,
633 Manning, A. J., Ray, E., Rigby, M., Hall, B. D., Siso, C., Nance, J. D., Krummel, P. B., Mühle, J.,
634 Young, D., O'Doherty, S., Salameh, P. K., Harth, C. M., Prinn, R. G., Weiss, R. F., Elkins, J. W.,
635 Walter-Terrinoni, H., and Theodoridi, C.: A decline in global CFC-11 emissions during
636 2018−2019, Nature, 590, 428-432, 10.1038/s41586-021-03260-5, 2021.

637 Nehrkorn, T., Eluszkiewicz, J., Wofsy, S., Lin, J., Gerbig, C., Longo, M., and Freitas, S.: Coupled
638 weather research and forecasting–stochastic time-inverted lagrangian transport (WRF–STILT)
639 model, Meteorology and Atmospheric Physics, 107, 51-64, 10.1007/s00703-010-0068-x, 2010.

640 Park, S., Western, L. M., Saito, T., Redington, A. L., Henne, S., Fang, X., Prinn, R. G., Manning,
641 A. J., Montzka, S. A., Fraser, P. J., Ganesan, A. L., Harth, C. M., Kim, J., Krummel, P. B., Liang,
642 Q., Mühle, J., O'Doherty, S., Park, H., Park, M.-K., Reimann, S., Salameh, P. K., Weiss, R. F.,
643 and Rigby, M.: A decline in emissions of CFC-11 and related chemicals from eastern China,
644 Nature, 590, 433-437, 10.1038/s41586-021-03277-w, 2021.

645 Ray, E. A., Portmann, R. W., Yu, P., Daniel, J., Montzka, S. A., Dutton, G. S., Hall, B. D., Moore,
646 F. L., and Rosenlof, K. H.: The influence of the stratospheric Quasi-Biennial Oscillation on trace
647 gas levels at the Earth's surface, Nature Geoscience, 13, 22-27, 10.1038/s41561-019-0507-3,
648 2020.

649 Rigby, M., Park, S., Saito, T., Western, L. M., Redington, A. L., Fang, X., Henne, S., Manning,
650 A. J., Prinn, R. G., Dutton, G. S., Fraser, P. J., Ganesan, A. L., Hall, B. D., Harth, C. M., Kim, J.,
651 Kim, K. R., Krummel, P. B., Lee, T., Li, S., Liang, Q., Lunt, M. F., Montzka, S. A., Mühle, J.,
652 O'Doherty, S., Park, M. K., Reimann, S., Salameh, P. K., Simmonds, P., Tunnicliffe, R. L., Weiss,
653 R. F., Yokouchi, Y., and Young, D.: Increase in CFC-11 emissions from eastern China based on
654 atmospheric observations, Nature, 569, 546-550, 10.1038/s41586-019-1193-4, 2019.

655 Rodgers, C. D.: Inverse Methods for Atmospheric Sounding, World Sci., Oxford, 10.1142/3171,
656 2000.

657 Say, D., Ganesan, A. L., Lunt, M. F., Rigby, M., O'Doherty, S., Harth, C., Manning, A. J.,
658 Krummel, P. B., and Bauguitte, S.: Emissions of halocarbons from India inferred through

659 atmospheric measurements, Atmos. Chem. Phys., 19, 9865-9885, 10.5194/acp-19-9865-2019,
660 2019.

661 Simpson, I. J., Blake, D. R., Barletta, B., Meinardi, S., Blake, N. J., Wang, T., Yang, L., Stone, E.
662 A., Yokelson, R. J., Farrukh, M. A., Aburizaiza, O. S., Khwaja, H., Siddique, A., Zeb, J., Woo, J.
663 H., Kim, Y., Diskin, G. S., and Peterson, D. A.: Recent CFC-11 Enhancements in China, Nepal,
664 Pakistan, Saudi Arabia and South Korea, American Geophysical Union, Fall Meeting 2019, San
665 Francisco, CO, USA, December 01, 2019, 2019AGUFM.A33T2896S, A33T-2896, 2019.

666 Stein, A. F., Draxler, R. R., Rolph, G. D., Stunder, B. J. B., Cohen, M. D., and Ngan, F.: NOAA's
667 HYSPLIT atmospheric transport and dispersion modeling system, Bulletin of the American
668 Meteorological Society, 10.1175/BAMS-D-14-00110.1, 2015.

669 United Nations Environment Programme (UNEP): Executive Committee of the Multilateral Fund
670 for the Implementation of the Montreal Protocol, Eighty-third Meeting. Addendum: Reports On
671 Projects With Specific Reporting Requirements., 2019.

672 United Nations Environment Programme (UNEP): Consumption of controlled substances
673 [dataset], 2021a.

674 United Nations Environment Programme (UNEP): Production of controlled substances [dataset],
675 2021b.

676 Wofsy, S. C., S. Afshar, H.M. Allen, E.C. Apel, E.C. Asher, B. Barletta, J. Bent, H. Bian, B.C.
677 Biggs, D.R. Blake, N. Blake, I. Bourgeois, C.A. Brock, W.H. Brune, J.W. Budney, T.P. Bui, A.
678 Butler, P. Campuzano-Jost, C.S. Chang, M. Chin, R. Commane, G. Correa, J.D. Crounse, P. D.
679 Cullis, B.C. Daube, D.A. Day, J.M. Dean-Day, J.E. Dibb, J.P. DiGangi, G.S. Diskin, M. Dollner,
680 J.W. Elkins, F. Erdesz, A.M. Fiore, C.M. Flynn, K.D. Froyd, D.W. Gesler, S.R. Hall, T.F. Hanisco,
681 R.A. Hannun, A.J. Hills, E.J. Hintsa, A. Hoffman, R.S. Hornbrook, L.G. Huey, S. Hughes, J.L.
682 Jimenez, B.J. Johnson, J.M. Katich, R.F. Keeling, M.J. Kim, A. Kupc, L.R. Lait, J.-F. Lamarque,
683 J. Liu, K. McKain, R.J. Mclaughlin, S. Meinardi, D.O. Miller, S.A. Montzka, F.L. Moore, E.J.
684 Morgan, D.M. Murphy, L.T. Murray, B.A. Nault, J.A. Neuman, P.A. Newman, J.M. Nicely, X.
685 Pan, W. Paplawsky, J. Peischl, M.J. Prather, D.J. Price, E.A. Ray, J.M. Reeves, M. Richardson,
686 A.W. Rollins, K.H. Rosenlof, T.B. Ryerson, E. Scheuer, G.P. Schill, J.C. Schroder, J.P. Schwarz,
687 J.M. St.Clair, S.D. Steenrod, B.B. Stephens, S.A. Strode, C. Sweeney, D. Tanner, A.P. Teng, A.B.
688 Thames, C.R. Thompson, K. Ullmann, P.R. Veres, N. Vieznor, N.L. Wagner, A. Watt, R. Weber,
689 B. Weinzierl, P.O. Wennberg, C.J. Williamson, J.C. Wilson, G.M. Wolfe, C.T. Woods, and L.H.
690 Zeng: ATom: Merged Atmospheric Chemistry, Trace Gases, and Aerosols [dataset],
691 https://doi.org/10.3334/ORNLDAAC/1581, 2018.

692
693
694
695
696
697
698
699
700

Table 1. Global and regional emissions (Gg yr^{-1}) derived from this analysis for Nov 2009 – Sep 2011 and Aug 2016 – May 2018 and the derived emission increases between the two periods (left columns). Two types of uncertainties were given in the parentheses. The former range indicates the 2.5^{th} – 97.5^{th} percentile range of the mean estimates derived from the 23 inversion ensembles. The latter range indicates the 2.5^{th} – 97.5^{th} percentile range of the 23 inversions, considering the mean and 2σ errors from each inversion. The right columns indicate the percentage contributions of regional emission to the global CFC-11 emissions and emission changes; values in the parentheses indicate the 2.5^{th} – 97.5^{th} percentile range of the mean regional emissions relative to the mean global emissions among the 23 inversion ensembles.

| Region	Nov 2009 - Sep 2011		Aug 2016 - May 2018		Change	
	Emissions	Percentage	Emissions	Percentage	Emissions	Percentage
Global	56 (49 – 68; 39 - 75)	100	84 (78 – 101; 67 – 113)	100	29 (21 – 40; 5 – 56)	100
Continents						
N. America	5.9 (5.6 – 7.1; 4.4 - 8.5)	11 (9 - 14)	5.6 (5.1 – 7.5; 3.5 – 9.6)	7 (6 - 9)	-0.4 (-2 – 1; -4 - 4)	-1 (-5 - 5)
S. America	6 (5 – 10; 1 - 16)	11 (9 - 16)	9 (7 – 18; 3 - 25)	11 (8 - 18)	3 (-2 – 11; -9 – 19)	8 (-9 - 27)
Africa	10 (7 – 14; 1 - 23)	17 (13 - 24)	9 (7 – 14; 2 - 24)	11 (8 - 15)	-1 (-6 – 5; -17 – 15)	-3 (-26 - 14)
Asia	24 (21 – 33; 14 - 40)	43 (37 - 52)	48 (45 – 56; 38 - 65)	57 (49 - 62)	24 (18 – 28; 8 - 39)	86 (59 - 115)
Europe	9 (5 – 11; 2 - 15)	15 (11 - 20)	11 (7 – 15; 4 - 18)	12 (9 - 16)	2 (-2 – 5; -7 - 10)	7 (-7 - 19)
Australia	0.5 (0.4 – 2; -1 - 4)	1 (1-3)	1 (0.6 – 6; 0.1 - 10)	1 (1-7)	0.7 (-1 – 6; -4 - 11)	2 (-4 - 16)
Asian Subregions						
Boreal Asia	0.6 (0.2 – 3; 0.1 - 5)	1 (0 - 6)	0.8 (0.4 – 3; 0.1 - 4)	1 (0 - 3)	0.1 (-3 – 2; -4 - 4)	0 (-11 - 8)
Temperate E. Asia	10 (8 – 13; 5 – 16)	18 (15 - 21)	14 (12 – 18; 9 - 22)	17 (14 - 23)	4 (2 – 8; -3 - 12)	15 (6 - 34)
Temperate W. Asia	6 (4 – 10; -3 - 16)	10 (7 - 14)	16 (12 – 20; 5 - 29)	19 (15 - 23)	10 (6 – 13; -3 - 24)	36 (25 - 56)
Tropical Asia	8 (6 – 11; 2 - 16)	14 (11 - 18)	18 (16 – 23; 11 - 29)	21 (17 - 25)	10 (5 – 14; -2 - 22)	35 (22 - 51)

712 **Table 2.** Comparison of regional emissions derived from this study and reported by previous top-
713 down analyses.

Regions	Time Periods	Emissions (Gg/y)	References
Asia			
Eastern Mainland China	2008 - 2012	5 – 13 [1]	Rigby et al., 2019; Park et al., 2021
Temperate Eastern Asia	Nov 2009 - Sep 2011	10 (5 - 16)	This Study
Eastern Mainland China	2014 - 2017	12 – 20 [1]	Rigby et al., 2019; Park et al., 2021
Eastern China	2014 - 2018	19 $\pm$ 5	Adcock et al., 2020
Temperate Eastern Asia	Aug 2016 - May 2018	14 (9 - 22)	This Study
Europe			
35º - 55ºN; -10º - 30ºE	2009	4.2 (2.9 - 5.4)	Keller et al., 2011
35º - 70ºN; -10º - 60ºE	Nov 2009 - Sep 2011	10 (6 - 16)	This Study
Australia			
Australia	2010 - 2017	0.32 $\pm$ 0.04	Fraser et al., 2021
Australia	Nov 2009 - Sep 2011	0.4 (0 - 0.8)	This study
Australia	Aug 2016 - May 2018	0.6 (0.1 - 1.6)	This study
North America			
The contiguous US	2009 - 2011	8.2 $\pm$ 1.0	Hu et al., 2017
North America	Nov 2009 - Sep 2011	5.9 (4.4 - 8.5)	This study
The contiguous US	2014	4.5 $\pm$ 0.7	Hu et al., 2017
North America	Aug 2016 - May 2018	5.6 (3.5 - 9.6)	This study

714 Notes: [1]values were taken from the reported inversion ensemble spread.
715
716
717
718
719
720
721
722
723
724
725
726
727
728
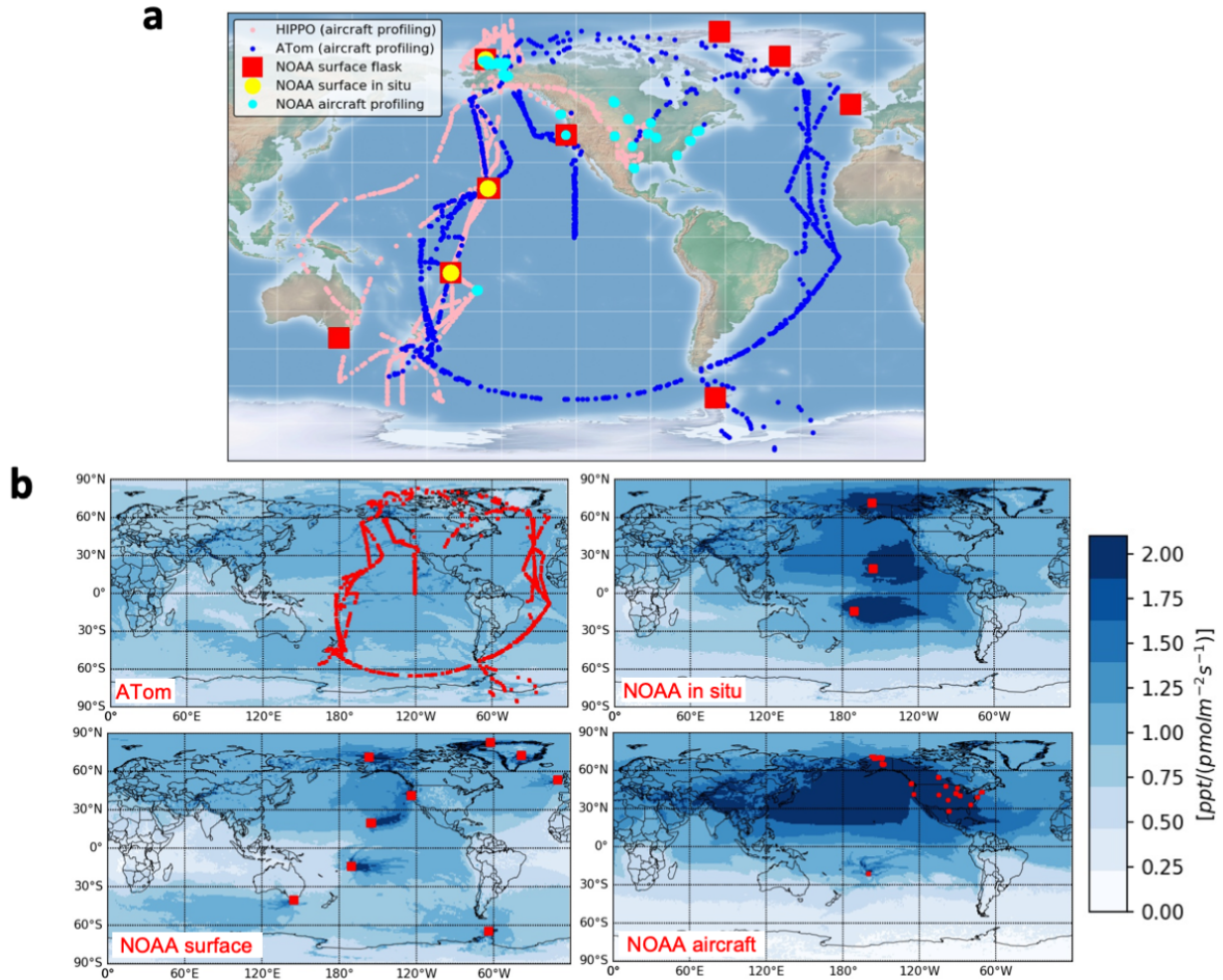
729
730 **Fig. 1.** Global atmospheric CFC-11 observations considered in this study (upper panel), including
731 selected flask measurements from the NASA HIPPO and ATom campaigns, observations from the
732 NOAA global weekly surface flask sampling network, NOAA global in situ surface sampling
733 network, and NOAA aircraft profiling sites. The bottom four panels indicate the summed footprints
734 between Aug 2016 – May 2018 from ATom (number of observations: 1003), NOAA weekly
735 surface flask network (number of observations: 781), in situ network (only selected $1-2$ samples
736 per day; number of observations: 2559), and biweekly – monthly aircraft profiling sites (only data
737 above 1 km above ground were selected at North American sites; number of observations: 4824).
738
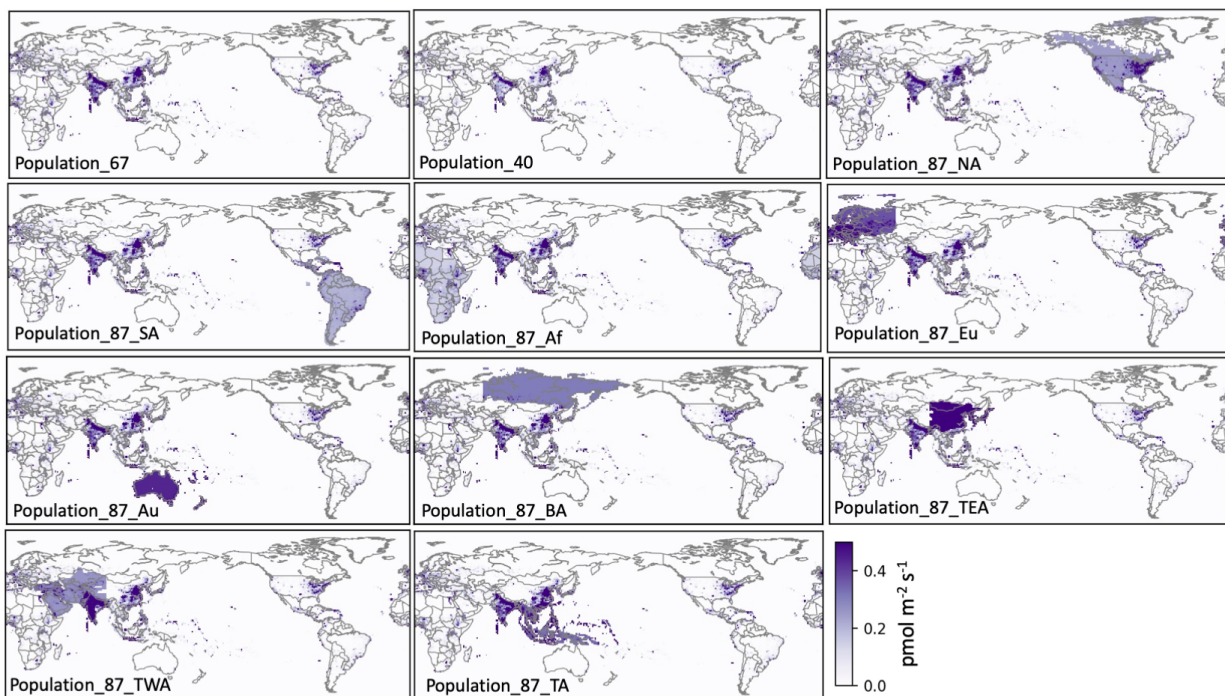
739
740 **Fig. 2**. Prior CFC-11 emissions used in this study. Priors of "population_67" and "population_40"
741 have global CFC-11 emissions of 67 Gg yr^{-1} and 40 Gg yr^{-1}. Compared to the prior
742 "population_67", priors of "population_87_NA", "population_87_SA", "population_87_Af",
743 "population_87_Eu", "population_87_Au", "population_87_BA", "population_87_TEA",
744 "population_87_TWA", and "population_87_TA" have a global emission total of 87 Gg yr^{-1} with
745 additional 20 Gg yr^{-1} emissions imposed over North America, South America, Africa, Europe,
746 Australia, boreal Asia, temperate eastern Asia, temperate western Asia, and tropical Asia,
747 respectively.
748
749
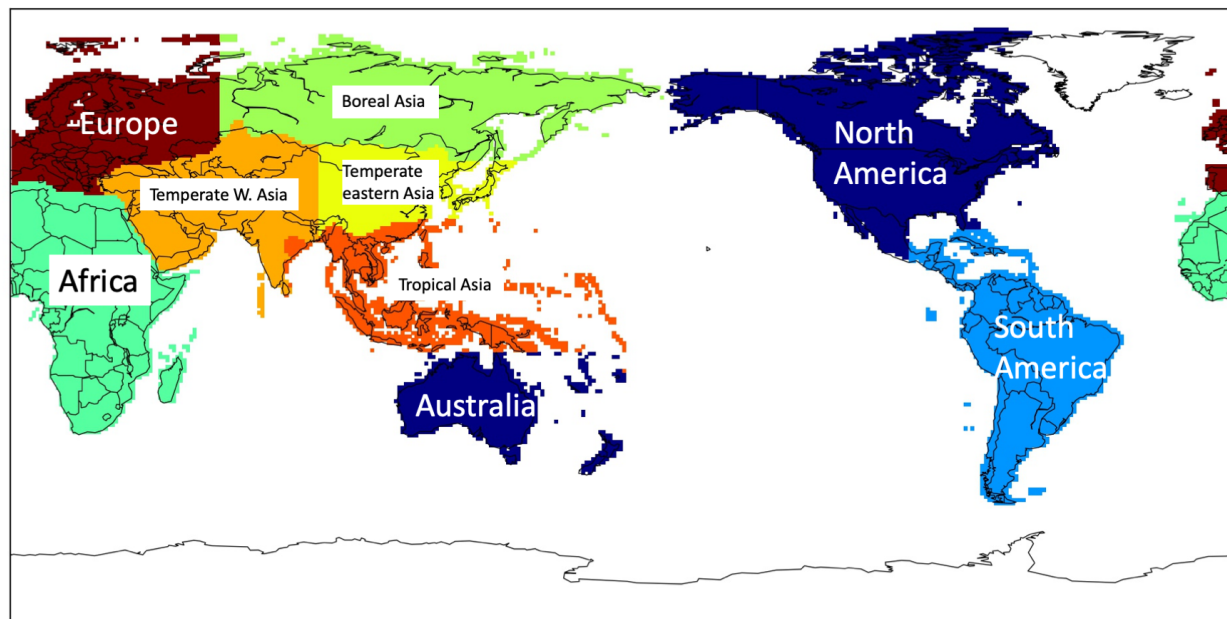
Fig. 3. Emissive regions defined for this analysis: North America, South America, Europe, Africa, Australia, and Asia; Asia was further divided into Boreal Asia, Temperate Eastern Asia, Temperate Western Asia, and Tropical Asia.
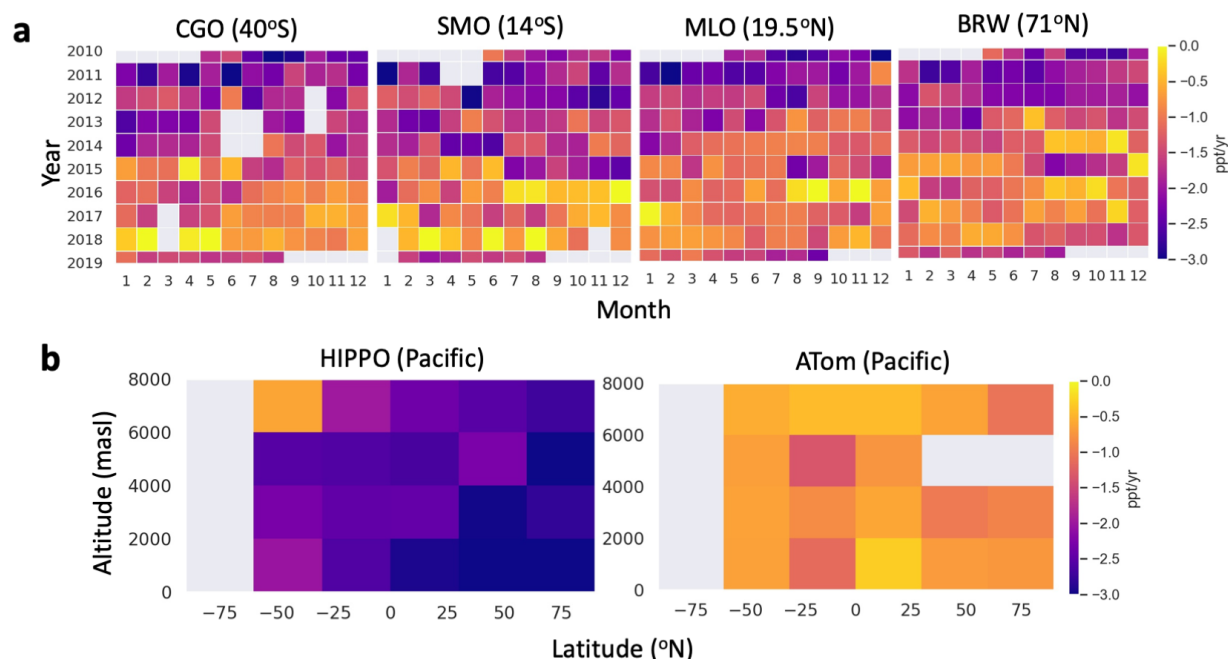
762
763 **Fig. 4**. Annual growth rates of atmospheric CFC-11 measured at four surface flask sampling sites
764 over the Pacific Ocean basin from 2010 – 2019 (a) and CFC-11 growth rates measured during the
765 selected HIPPO and ATom aircraft profiling surveys that took place during Nov 2009 - Sep 2011
766 and Aug 2016 - May 2018, respectively (b). Each grid cell indicates an annual difference relative
767 to the prior year for that given month (in panel a) or location (in panel b). Gray cells indicate
768 periods or locations with no data. The four surface sites plotted in panel (a) are Cape Grim,
769 Tasmania, Australia (CGO), Tutuila, American Samoa (SMO), Mauna Loa, Hawaii, United States
770 (MLO), and Pt. Barrow, Alaska, United States (BRW).
771
772
773
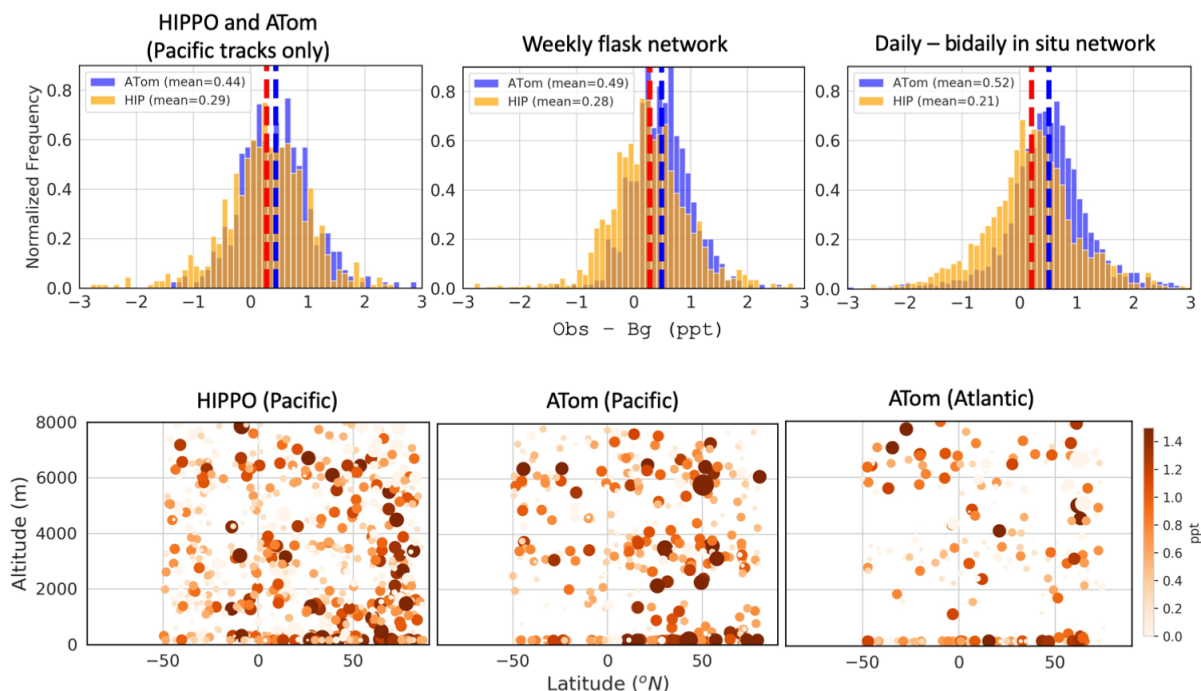
774
775 **Fig. 5**. Enhancements of CFC-11 mole fractions relative to background air mole fractions,
776 measured by three independent networks during Nov 2009 – Sep 2011 (HIPPO period) and Aug
777 2016 – May 2018 (ATom period). (a) Histograms of enhancements of CFC-11 mole fractions
778 measured from flasks collected over the Pacific Ocean basin during the HIPPO and ATom
779 campaigns (left panel), in flasks collected in the NOAA weekly surface sampling network during
780 those periods (middle panel), and measured from the NOAA in situ sampling network in both
781 periods (right panel). Orange bars indicate normalized frequencies of enhancements observed in
782 the HIPPO period, whereas blue bars indicate normalized frequencies of enhancements observed
783 in the ATom period. Red and blue dashed lines denote the mean mole fractions observed during
784 HIPPO and ATom periods. (b) Atmospheric CFC-11 mole fraction enhancements measured from
785 flasks above the Pacific Ocean Basin during HIPPO (left) and ATom (middle), and above the
786 Atlantic Ocean Basin during ATom (right). Both color shading and size of the symbols are
787 proportional to the magnitude of mole fraction enhancements.
788
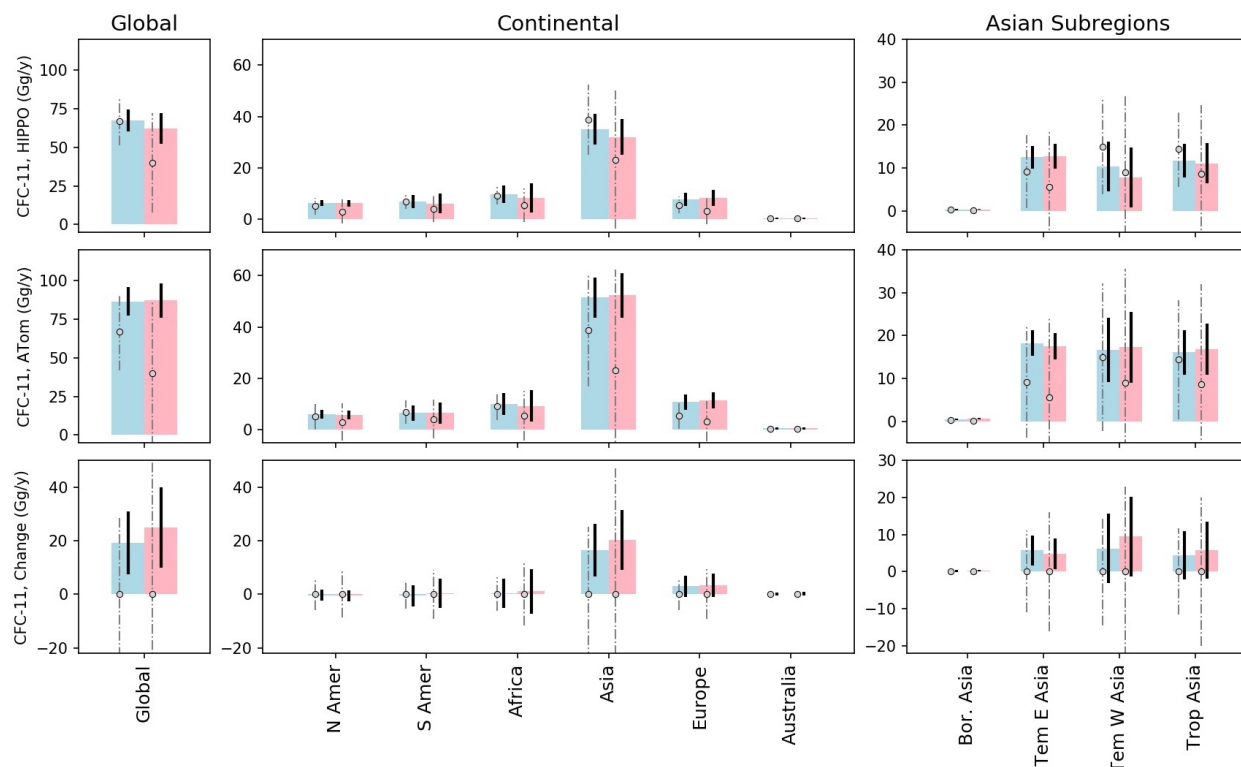
789
790 **Fig. 6.** Prior (circles) and posterior (bars) CFC-11 emissions derived for the globe, continents, and
791 Asian subregions, from the "flask-only" inversions for the HIPPO period (upper three panels), the
792 ATom period (middle three panels), and emission differences between the two periods (lower three
793 panels). In each region and from the left to right, open circles denote the two assumed prior
794 emissions ("population_67" and "population 40") with zero changes between the HIPPO and
795 ATom periods. Gray dashed lines indicate 2σ prior uncertainties. Light blue and pink bars
796 correspond to posterior emissions derived from the two different priors. Black errorbars of CFC-
797 11 emissions derived for the HIPPO and ATom periods (the upper and middle panels) indicate 2σ
798 posterior uncertainties derived from individual inversions. Errorbars for the derived CFC-11
799 emission changes (the lower panels) between the HIPPO and ATom periods were calculated from
800 the square root of the sum squared errors shown in the upper and middle panels.
801

24
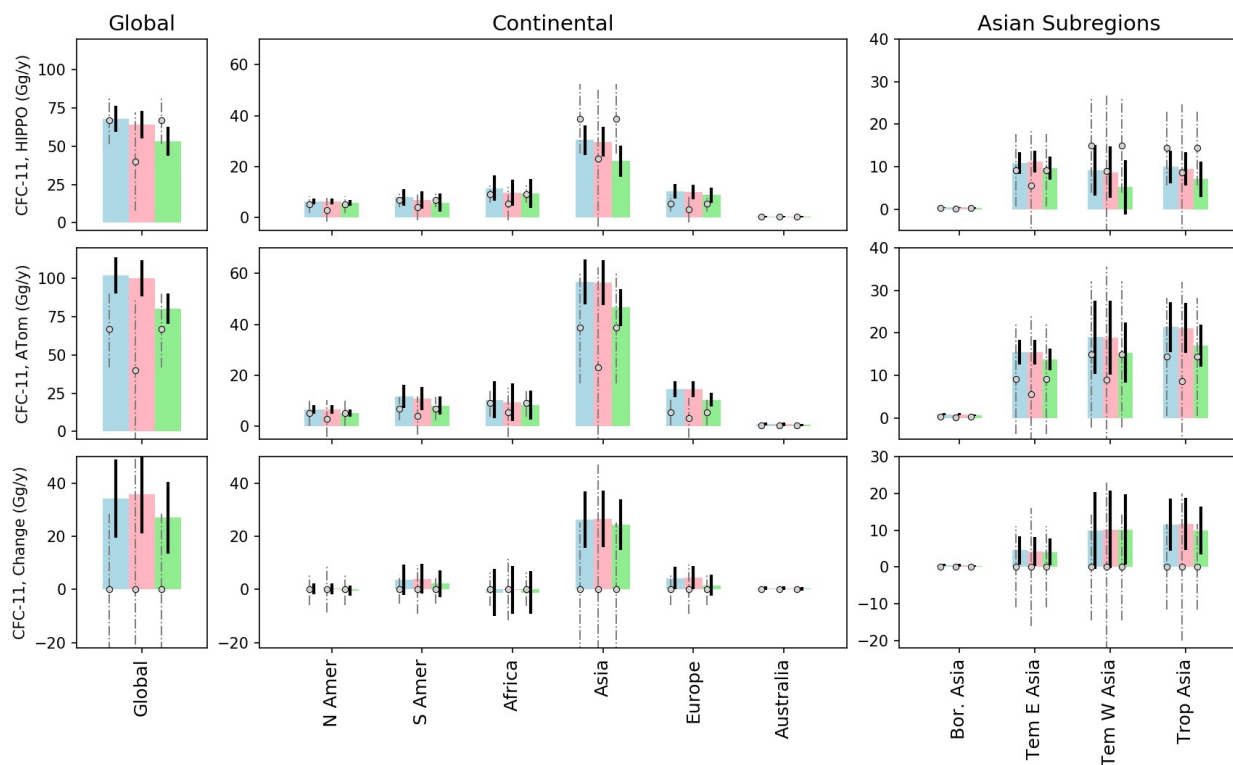
802
803 **Fig. 7.** Prior (circles) and posterior (bars) CFC-11 emissions derived for the globe, continents, and
804 Asian subregions, from the "flask + in situ" inversions for the HIPPO period (upper three panels),
805 the ATom period (middle three panels), and emission differences between the two periods (lower
806 three panels). In each region and from the left to right, open circles denote the three assumed prior
807 emissions ("population_67", "population 40", and "population_67") with zero changes between
808 the HIPPO and ATom periods. Light blue, pink, and green bars indicate posterior emissions
809 derived from the three priors and two different backgrounds, as described in inversions ID = 3 - 5
810 in Table S1.
811
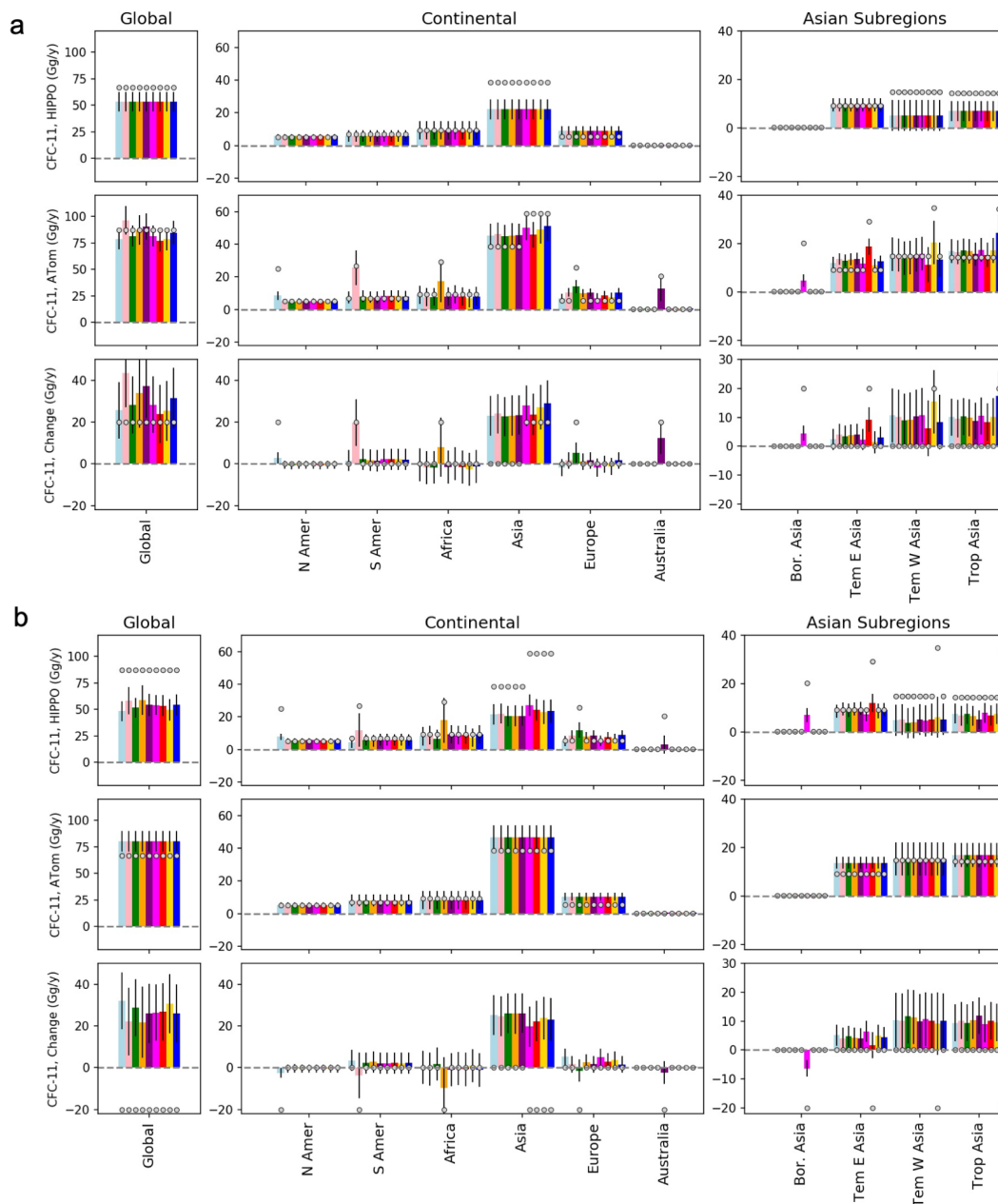
812
Fig. 8. Testing the sensitivity of assumed prior emission changes on the inversion-derived emission changes. (a) Assume a 20 Gg yr^{-1} emission increase between the HIPPO and ATom periods in individual continents and Asian subregions. (b) Assume a 20 Gg yr^{-1} emission decrease between the HIPPO and ATom periods in individual continents and Asian subregions. Similar to Fig. 7, posterior CFC-11 emissions were derived from the "flask + in situ" inversions for the HIPPO and the ATom periods. In each region and from the left to right, open circles denote the prior emissions as described for inversions ID = 6 - 14 in Table S1 for panel (a), and for inversions ID = 15 - 23 in Table S1 for panel (b); different colored bars indicate the corresponding posterior emissions derived from inversions ID = 6 - 14 (a) and ID = 15 - 23 (b) as described in Table S1.